Sustainable synthesis of composite ceramics using in situ synchrotron X-ray diffraction for effective immobilization of Sr-90 and its fission products

E. K. Papynov[1] · A. A. Belov[1] · O. O. Shichalin[1] · A. P. Zavjalov[2] · I. Yu. Buravlev[1] · A. N. Drankov[1] · S. A. Azon[1] · A. N. Fedorets[1] · A. A. Buravleva[1] · S. B. Yarusova[3] · V. Yu. Mayorov[1,4] · N. B. Kondrikov[1] · I. G. Tananaev[1,5] · V. I. Sergienko[6]

Abstract

In this work the method of obtaining composite ceramics based on perovskite and pyrochlore of compositions $Y_xZr_xSr_{1-3x}TiO_3$ (x = 0.1, x = 0.2, x = 0.3) and $Y_2(Zr_xTi)_2O_7$ (x = 1) using the technology of reactive spark plasma sintering has been investigated. A comprehensive study of phase transformations, structure formation and physical and mechanical characteristics of ceramics depending on the ratio of $Sr^{2+}/Y^{3+}/Zr^{4+}$ has been carried out by XRD, SEM, EDS and "diffraction movie" methods at the synchrotron radiation source. High hydrolytic stability of ceramics is proved and the mechanism of low leaching rate of $Sr^{2+} < 10^{-7}$ g cm^{-2} day, Y^{3+} and $Zr^{4+} < 10^{-5}$ g cm^{-2} day is described, which corresponds to GOST R 50926-96 and ANSI/ANS 16.1. The results of the work are promising for conditioning of radioactive waste and production of radioisotope products.

✉ O. O. Shichalin
oleg_shich@mail.ru

1   Far Eastern Federal University, 10 Ajax Bay, Russky Island, Vladivostok, Russia 690922

2   Synchrotron Research Department, Synchrotron Radiation Facility SKIF, Boreskov Institute of Catalysis Siberian Branch Russian Academy of Sciences, 1, Pr. Nikolsky, R.P. Koltsovo, Novosibirsk Region, Russian Federation 630559

3   Vladivostok State University, Gogolya, 41, Vladivostok, Russian Federation 690014

4   Far Eastern Geological Institute, Russian Academy of Sciences, 100 Let Vladivostok Avenue 159, Vladivostok, Russian Federation 690000

5   Kola Science Center, Tananaev Institute of Chemistry and Technology of Rare Elements and Mineral Raw Materials, Russian Academy of Sciences, Akademgorodok, 26a, Apatity, Russian Federation 184209

6   Presidium of the Far Eastern Branch of the Russian Academy of Sciences, Svetlanskaya, 50, Vladivostok, Russian Federation 690000

Graphical Abstract
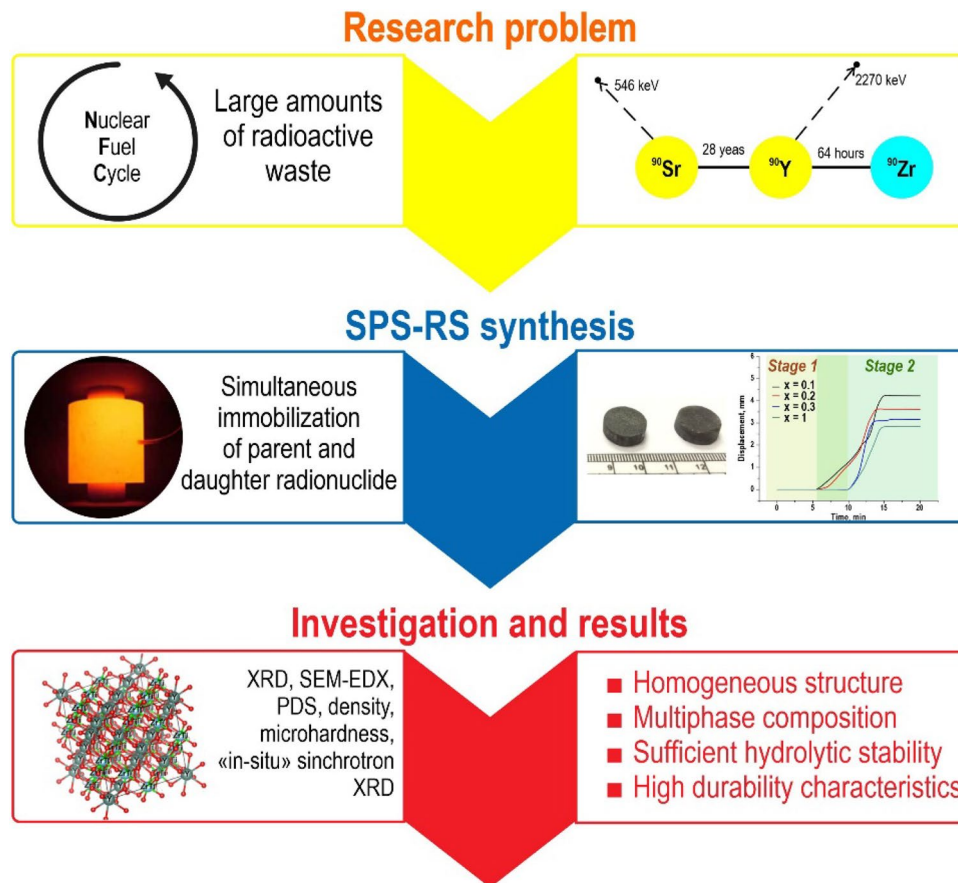
Introduction

Nuclear reactors and nuclear fuel cycle facilities annually generate millions of tons of solid and liquid radioactive waste (RAW) of various activity levels [1–3]. A significant portion of this waste consists of long-lived radionuclides, particularly ^{137}Cs, ^{90}Sr, and others, including their fission products, which pose a threat of radioactive contamination to the environment [4, 5]. The management of these radionuclides, especially ^{90}Sr, is of crucial importance due to its long half-life (28.8 years) and high decay energy. Specifically, ^{90}Sr is a β-emitter with an energy of 0.546 MeV, which decays into ^{90}Y—a high-energy (2.28 MeV) β-emitter with a half-life of 64 h. In turn, ^{90}Y decays into stable ^{90}Zr. In this context, developing an approach for the joint immobilization of radionuclides and the stable isotope ^{90}Zr in a single inert matrix capable of reliably containing them for an extended period is an extremely important task. This challenge is associated with several difficulties described below.

The diverse chemical properties of radionuclides ^{90}Sr and ^{90}Y, including the stable isotope ^{90}Zr, complicate the selection of a material capable of simultaneously and effectively binding them within its volume. The high energy of β-radiation emitted by these radionuclides can lead to radiation damage and degradation of the immobilizing matrix. Additionally, radiation-induced heating may initiate thermal decomposition of the matrix. Hydrolytic exposure can cause chemical and mechanical instability of the binding matrix material.

In recent years, a large number of studies on the immobilization of radioactive waste containing long-lived radionuclides such as ^{90}Sr, ^{137}Cs, and others have focused on exploring the potential use of ceramic materials with mineral-like compositions. Mineral-like ceramics refer to synthetic analogues of natural minerals capable of incorporating radionuclides into their crystal structure and ensuring their

reliable immobilization. The most promising ceramics of this type include aluminosilicates [6, 7], phosphates [8–10], perovskites (isostructural with $CaTiO_3$) [11–13], feldspars [14, 15], scheelites ($CaWO_4$), and others. Several studies [16, 17] have demonstrated the high effectiveness of ceramic matrices with mineral-like compositions, synthesized by various methods, for the incorporation of actinides and fission products. Particular attention is given to ceramics with SYNROC structure and pyrochlores, which can effectively incorporate radionuclides such as ^{137}Cs and ^{90}Sr through isomorphic substitution of cations in the crystal lattices of the ceramics. This ensures low leaching rates of radionuclides (10^{-5}–10^{-7} g cm^{-2} day), high accumulation capacity, and radiation resistance of these ceramics [18, 19].

It is important to note that the final properties of ceramic matrices for radioactive waste immobilization are influenced not only by their composition but also by the method of synthesis. Traditional ceramic production methods, such as hot pressing, reaction sintering, and others [20–22], typically involve high processing temperatures (ranging from 1400 to 1600 °C) and long holding cycles (from several hours to days). This leads to significant energy consumption, potential formation of secondary waste in the gas phase, reduced quality of the final product, and equipment wear. Moreover, ceramic materials obtained by these methods often exhibit low quality—they have increased open porosity, heterogeneous microstructure, insufficient density, and low mechanical strength [22, 23].

An effective solution to the aforementioned problems requires the application of modern materials and methods, including fundamental research to improve existing technologies. In particular, our recent study [24] examined and implemented an unconventional method of solid-phase synthesis of mineral-like composite ceramics based on perovskite $SrTiO_3$ and pyrochlore $Y_2Ti_2O_7$ for the immobilization of radionuclides ^{90}Sr and its daughter radionuclide ^{90}Y, as well as lanthanides and actinides, using reactive spark plasma sintering (SPS-RS) technology. The creation of the composite ceramic matrix took into account the dual nature of ^{90}Sr's existence together with its fission product ^{90}Y, which requires control of the structural and phase state of the composite depending on the varying Sr^{2+}/Y^{3+} ratio in its composition. The key originality of the technological approach was the formation of ceramics with the required composite composition through reactive "in situ" interaction of the reaction mixture (RM) of oxides with the composition $Y_xSr_{1-1.5x}TiO_3$ (x = 0.2, 0.4, 0.6 and 1) during spark plasma heating. As a result of optimizing the RM composition and SPS-RS modes, the formation of high-quality ceramic matrices was achieved under mild temperature and time sintering conditions, chemically binding Sr^{2+} and Y^{3+} in their volume within the structures of perovskite $SrTiO_3$ and pyrochlore $Y_2Ti_2O_7$, and meeting the requirements of

GOST R 50926-96 and ANSI/ANS 16.1 for solidified high-level waste.

However, it should be noted that the radioactive decay chain of ^{90}Sr is not limited to ^{90}Y, but proceeds with the formation of ^{90}Zr. Thus, when immobilizing ^{90}Sr, the presence of ^{90}Y and ^{90}Zr in the matrix material should be considered, which requires control of its structural and phase state, which will determine key performance characteristics. In this regard, the aim of the present work was to study the solid-phase synthesis of mineral-like ceramics containing strontium, based on perovskite $SrTiO_3$ in composition with the addition of Y^{3+} and Zr^{4+} with various $Sr^{2+}/Y^{3+}/Zr^{4+}$ ratios, using SPS-RS technology. The research is supported by studying the kinetics of phase transformations during the interaction of RM components over time using X-ray diffraction analysis (XRD) on a synchrotron radiation (SR) source under "in situ" heating conditions (heating synchrotron XRD experiment). This makes it possible to establish the temperature intervals of phase formation, evaluate the rates of solid-phase reactions, identify possible intermediate compounds in the ceramic composition, and determine their influence on its performance characteristics. Establishing optimal synthesis modes will allow obtaining materials with adjustable properties necessary for reliable immobilization of ^{90}Sr, ^{90}Y, and ^{90}Zr. Such studies have not been conducted before.

Experimental

Experimental design

The experimental work consisted of 6 sequential stages (Fig. 1): *Stage 1*—preparation of starting powders of composite mixtures for four samples with different values of the stoichiometric coefficient for zirconium (x = 0.1, 0.2, 0.3, and 1.0); *Stage 2*—production of ceramic samples from the powder mixtures prepared in *Stage 1* using SPS-RS technology; *Stage 3*—preparation of ceramic samples for investigation (grinding, polishing); *Stage 4*—investigation of the structural properties of the obtained ceramics; *Stage 5*—investigation of the physical and mechanical properties of the obtained ceramics; *Stage 6*—evaluation of the hydrolytic stability of the ceramic samples.

Synthesis of initial reaction powder mixtures

The following initial components of "chemically pure" grade were used for experimental work on obtaining ceramic materials for the immobilization of ^{90}Sr, ^{90}Y, and ^{90}Zr: yttrium oxide (Y_2O_3), titanium oxide (TiO_2), strontium carbonate ($SrCO_3$), and zirconium oxide (ZrO_2) produced by Sigma-Aldrich (USA) with a mass fraction of the main substance > 99.99%.
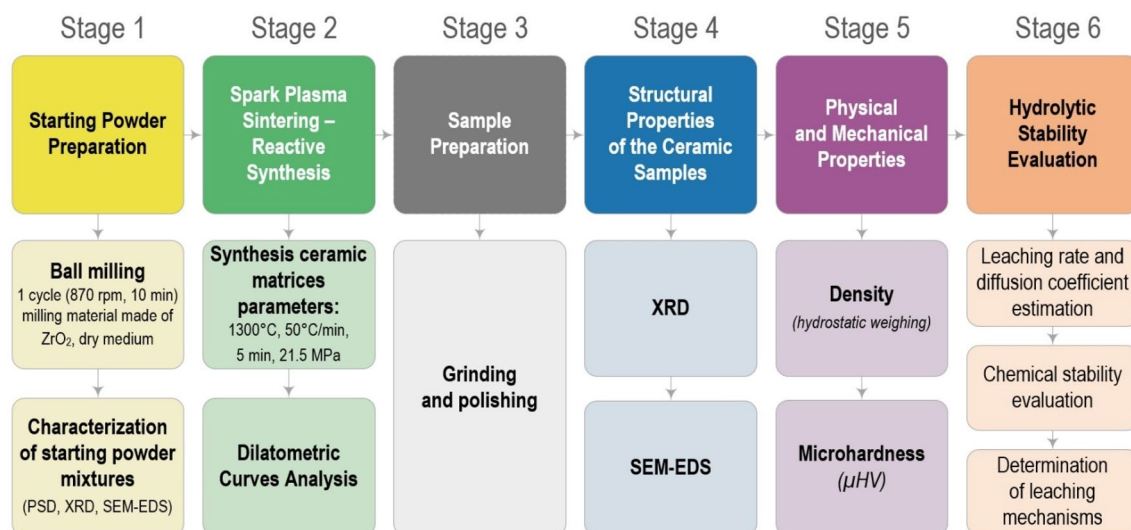
Fig. 1 Schematic of the experimental work

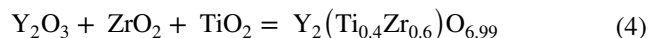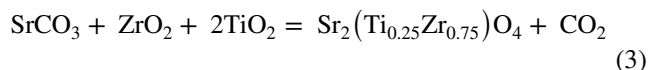**Table 1** Composition of initial reaction mixtures

Stoichiometric composition	Stoichiometric coefficient for Zr	Initial reagents in the starting powder mixture, g			
		$SrCO_3$	Y_2O_3	ZrO_2	TiO_2
$Sr_{0.7}Y_{0.1}Zr_{0.1}TiO_3$	0.1	5.89	0.64	0.35	4.55
$Sr_{0.4}Y_{0.2}Zr_{0.2}TiO_3$	0.2	3.54	1.35	1.47	4.78
$Sr_{0.1}Y_{0.3}Zr_{0.3}TiO_3$	0.3	0.93	2.13	2.20	5.03
$Y_2(Zr_xTi)_2O_7$	1.0	–	2.41	2.62	5.12

To compare the properties of ceramics of different compositions, the compositions of the initial reaction powder mixtures were calculated based on the condition of obtaining ceramics with stoichiometric formulas: (1) $Sr_{0.7}Y_{0.1}Zr_{0.1}TiO_3$, (2) $Sr_{0.4}Y_{0.2}Zr_{0.2}TiO_3$, (3) $Sr_{0.1}Y_{0.3}Zr_{0.3}TiO_3$ and (4) $Y_2(ZrTi)_2O_7$. The choice of these compositions is due to the promising application of perovskites and pyrochlores of similar composition as matrices for the immobilization of actinides and their fission products [25–27]. The masses of the components in the powder mixtures are presented in Table 1.

Homogenization of the initial powder mixtures was carried out by mechanical dry ("solvent-free") grinding using a Tencan XQM-0.4A vertical planetary mill (China). The grinding was performed in a cyclic mode in a container with grinding media (balls) made of zirconium dioxide at a speed of 870 rpm for 10 min, followed by cooling (1 cycle). To intensify the grinding process and reduce the probability of grinding media jamming in the grinding container, balls of different diameters were used (20 balls with a diameter of 1 mm, 10 balls with a diameter of 10 mm).

Preparation of ceramic samples

The ceramics were produced using SPS-RS technology through *in-situ* reactive interaction of initial reaction powder mixtures according to the proposed reactions (Eqs. 1–4), which occur simultaneously during spark plasma heating:

$$SrCO_3 + TiO_2 = SrTiO_3 + CO_2 \quad (1)$$

$$Y_2O_3 + 2TiO_2 = Y_2Ti_2O_7 \quad (2)$$

$$SrCO_3 + ZrO_2 + 2TiO_2 = Sr_2(Ti_{0.25}Zr_{0.75})O_4 + CO_2 \quad (3)$$

$$Y_2O_3 + ZrO_2 + TiO_2 = Y_2(Ti_{0.4}Zr_{0.6})O_{6.99} \quad (4)$$

The SPS-515S spark plasma sintering system, manufactured by "Dr.Sinter-LAB™" (Japan), was utilized in the experiment. The sintering process represents a highly effective methodology for achieving material densities and mechanical properties that are close to theoretical values.

Initially, 4 g of the starting powder mixture was placed in a graphite mold with a working diameter of 15.5 mm. Pre-pressing at a pressure of 20.7 MPa provided an initial degree of compaction of the powder. Subsequently, the preform was placed in a vacuum chamber at a pressure of 10^{-5} atm, creating conditions for a clean and controlled sintering process.

The heating of the sintered material was carried out using a unipolar low-voltage pulsed current in an On/Off mode. This method, with a periodicity of 12 pulses followed by 2 pauses, ensured uniform temperature distribution and prevented overheating. The duration of the pulse packet was 39.6 ms, while the pauses lasted 6.6 ms. The temperature

during the process was monitored using an optical laser pyrometer (IR-AHS "Hitachi," Japan), which was focused on a hole located in the middle of the outer wall of the mold at a depth of 5.5 mm, allowing for precise tracking of temperature changes throughout the process.

To minimize the adhesion of the consolidated powder to the mold and plungers, a 200 µm thick graphite foil was used. This facilitated the easy extraction of the sample after sintering. The mold was wrapped in insulating material (graphite wool) to reduce heat losses, promoting more efficient heating and energy savings.

The sintering was conducted at a temperature of 1300 °C with a controlled heating rate: 300 °C/min up to 650 °C, and 50 °C/min above this temperature, which allowed for the control of diffusion and crystallization processes within the material. The samples were held at the maximum temperature for 5 min to achieve the desired degree of sintering, after which they were slowly cooled to room temperature over a period of 30 min. The pressing pressure during consolidation was maintained at 21.5 MPa, enabling the attainment of high density and strength in the resulting materials.

Preparation of ceramic samples before investigation

To remove graphite foil from the ceramic surface, initial rough polishing was performed using silicon carbide (SiC) abrasive sandpaper with CAMI grain sizes 80, 120, and 240 from "Allied High Tech Products, Inc." (USA). Fine polishing was then carried out using sandpaper with CAMI grain sizes 400, 600, 800, and 1200, followed by polishing with diamond colloidal suspension with particle sizes of 9, 3, 1 µm, and 0.04 µm from "Allied High Tech Products, Inc." (USA) on a MECATECH 234 "PRESI" (France) polishing machine.

Characterization methods

Particle size distribution of powders was determined using an Analysette-22 NanoTec/MicroTec/XT "FRITSCH" (Germany) laser particle analyzer. Each sample was measured 12 times, and the results were averaged.

Scanning electron microscopy (SEM) was performed on a CrossBeam 1540 XB "Carl Zeiss" (Germany) instrument equipped with a "Bruker" (Germany) energy-dispersive X-ray spectroscopy (EDS) attachment.

Diffraction studies of powders and alloys were conducted on a Colibri "Burevestnik" (Russia) X-ray diffractometer. CuKα1-Kα2 radiation (40 kV, 10 mA) with an average wavelength (λ) of 1.5418 Å was used. The signal was recorded by a Muthen2 detector with a Kβ Ni-filter, scanning angle range 20–100°, scanning step 0.0185° with a dwell time of 244 s at each point.

Vickers microhardness (HV) was measured at a load of 0.2 N on an HMV-G-FA-D "Shimadzu" (Japan) microhardness tester. To analyze the dispersion of microhardness values obtained by indentation of ceramic sample surfaces, box and whisker diagrams were plotted. This data visualization method has been successfully used in analyzing various types of ceramics [28–30], significantly expanding analytical capabilities, including processing results of instrumental indentation of ceramics compared to using only average microhardness values [31]. Based on the analysis of diagram parameters, conclusions were drawn about the variation of ceramic surface properties, microhardness dispersion in different surface areas of the material, and an assessment of the cumulative influence of various factors (composition, microstructure, technological modes) on the final mechanical characteristics of the samples.

Specific density of samples was determined by hydrostatic weighing on an "OHAUS Corporation Adventurer™" (USA) balance.

Visualization of structures produced by «VESTA» software, version 3. This software is distributed free of charge for academic, scientific, educational, and non-commercial users. The reference is [32].

"In situ" *synchrotron study of SrTiO₃*

In situ X-ray diffraction experiments with heating were conducted using synchrotron radiation (SR) at the 5-B "Diffraction Cinema" station of the VEPP-3 storage ring [33] at the SSTRC shared research center based on the VEPP-4–VEPP-2000 complex at the Budker Institute of Nuclear Physics SB RAS [34]. Diffractograms were recorded with an OD-3 one-dimensional detector [35]. The wavelength of monochromatic radiation was 1.51 Å in the scanning angle range 2θ 18–50 degrees. Samples were placed in a special furnace heated at a constant rate of 15 °C/min up to 400 °C and 5 °C/min up to 1000 °C. The exposure time of OD-3 was set to 60 s.

Evaluation of hydrolytic stability

The hydrolytic stability of matrices was evaluated by the leaching rate of Sr^{2+}, Y^{3+}, and Zr^{4+} ions during prolonged contact (30 days) with distilled water (pH 6.8) at room temperature (25 °C) under static conditions according to GOST R 52126-2003, analogous to ANSI/ANS 16.1, updated in accordance with an earlier version recommended by the IAEA (ISO 6961:1982). The concentration of strontium ions was determined by inductively coupled plasma mass spectrometry (ICP-MS) using an iCAP 7600 Duo "Thermo Scientific" (USA) spectrometer.

The leaching rate was calculated according to the following formula:

$$R_n^i = \frac{m_n^i}{M_o^i \times t_n \times S} \tag{4}$$

where R_n^i is the leaching rate of the i-th element (g/cm^2·day); m_n^i is the mass of the i-th element leached during the n-th time interval, g; M_0^i is the concentration of the i-th element in the matrix, g/g; **S** is the exposed surface area of the sample, cm^2; t_n is the duration of the n-th time interval, days.

The calculation of the effective diffusion coefficient (**De**) was carried out using mathematical transformations of Fick's second law according to the method described in [36]:

$$\frac{\sum m}{M_0} = 2\left(\frac{D_e}{\pi}\right)^{\frac{1}{2}} \times \left(\frac{S}{V}\right) t^{\frac{1}{2}} + \alpha \tag{5}$$

, where **m** is the mass of the element, mg; **t** is the leaching time, s; M_0 is the initial content of the element in the matrix, mg; D_e is the effective diffusion coefficient, cm^2/s; **S** is the exposed surface area of the sample, cm^2; **V** is the volume of the sample, cm^3; α is a parameter that takes into account the initial leaching of the element not related to diffusion (for example, strontium is leached during the initial contact of the contact solution with the sample surface).

In the calculation, this equation was brought to a linear form by introducing the coefficient **K**, which represents the tangent of the angle of inclination of the straight line of the dependence of strontium leaching from the sample on the square root of the contact time of the material with the leaching agent:

$$K = 2\left(\frac{D_e}{\pi}\right)^{0.5} \times \left(\frac{S}{V}\right) \tag{6}$$

The effective diffusion coefficient was calculated:

$$D_e = \frac{K^2 \times \pi}{4} \times \left(\frac{V}{S}\right)^2 \tag{7}$$

The leaching index (**L**) was calculated as the decimal logarithm of the inverse of diffusion:

$$L = lg\frac{1}{D_e} \tag{8}$$

Evaluation of the dominant leaching mechanism based on the dependence of the decimal logarithm of the accumulated fraction of leached radionuclide (**Bt**, mg/m^2) on the decimal logarithm of leaching time t, s:

$$lg(B_t) = \frac{1}{2}lgt + lg\left[U_{max}d\sqrt{\frac{D_e}{\pi}}\right] \tag{9}$$

, where U_{max} is the maximum amount of leached radionuclide, mg/kg, **d** is the density of the matrix, kg/m^3.

The leaching depth of the matrix characterizes the destruction of the matrix.

The matrix when in an aqueous environment is calculated by Eq. (10):

$$L_t^i = \sum_i^n \left(W_n^i \frac{t_n}{d}\right) \tag{10}$$

where L_t^i is the leaching depth of the matrix achieved over the time interval t_n, cm; **d** is the density of the sample, g/cm^3.

Results and discussion

Preparation of initial reaction powder mixtures and their investigation

To assess the quality of homogenization and the effect of ZrO_2 presence in the system (with varying content) on the grinding of components, an analysis of particle size distribution was conducted in their initial state (Fig. 2) and after mixing (Fig. 3a, b). As shown in Fig. 2, the initial powders of $SrCO_3$, TiO_2, Y_2O_3, and ZrO_2, when combined without subsequent grinding, have a wide fractional composition with particles in the size range from 0.1 to 100 μm (Fig. 2). The initial $SrCO_3$ powder (Fig. 2a) is characterized by a bimodal distribution with two peaks (1.5 μm and 40 μm). The fractional contribution curve shows that smaller particles (< 3 μm) constitute a significant part of the particle distribution in the fraction volume. For Y_2O_3 (Fig. 2b), the distribution is shifted towards larger particle sizes with three peaks around 3 μm, 13 μm, and 50 μm. For ZrO_2 (Fig. 3b), the distribution is unimodal with a distinct peak around 70 μm. For TiO_2 (Fig. 2d), the distribution is also shifted towards larger particle sizes with three characteristic peaks: 100 nm, 2.5 μm, 10 μm, and 35 μm.

As a result of homogenization, the granulometric composition undergoes a significant narrowing of the particle size range (to 0.1–1 μm) (Fig. 3a, b), which is primarily due to the abrasive effect of ZrO_2. Increasing the ZrO_2 content above x = 0.2 does not lead to further changes in the fractional distribution, indicating that the maximum possible degree of grinding has been achieved. SEM analysis (Fig. 3a*–d*) confirms the particle size range from 1 μm and less. EDS analysis (Fig. 3) indicates a homogeneous distribution of Sr^{2+} and Ti^{4+}.

Homogenization of the reaction mixtures under the specified parameters and duration of the mixing process does not affect the phase composition of the powder components
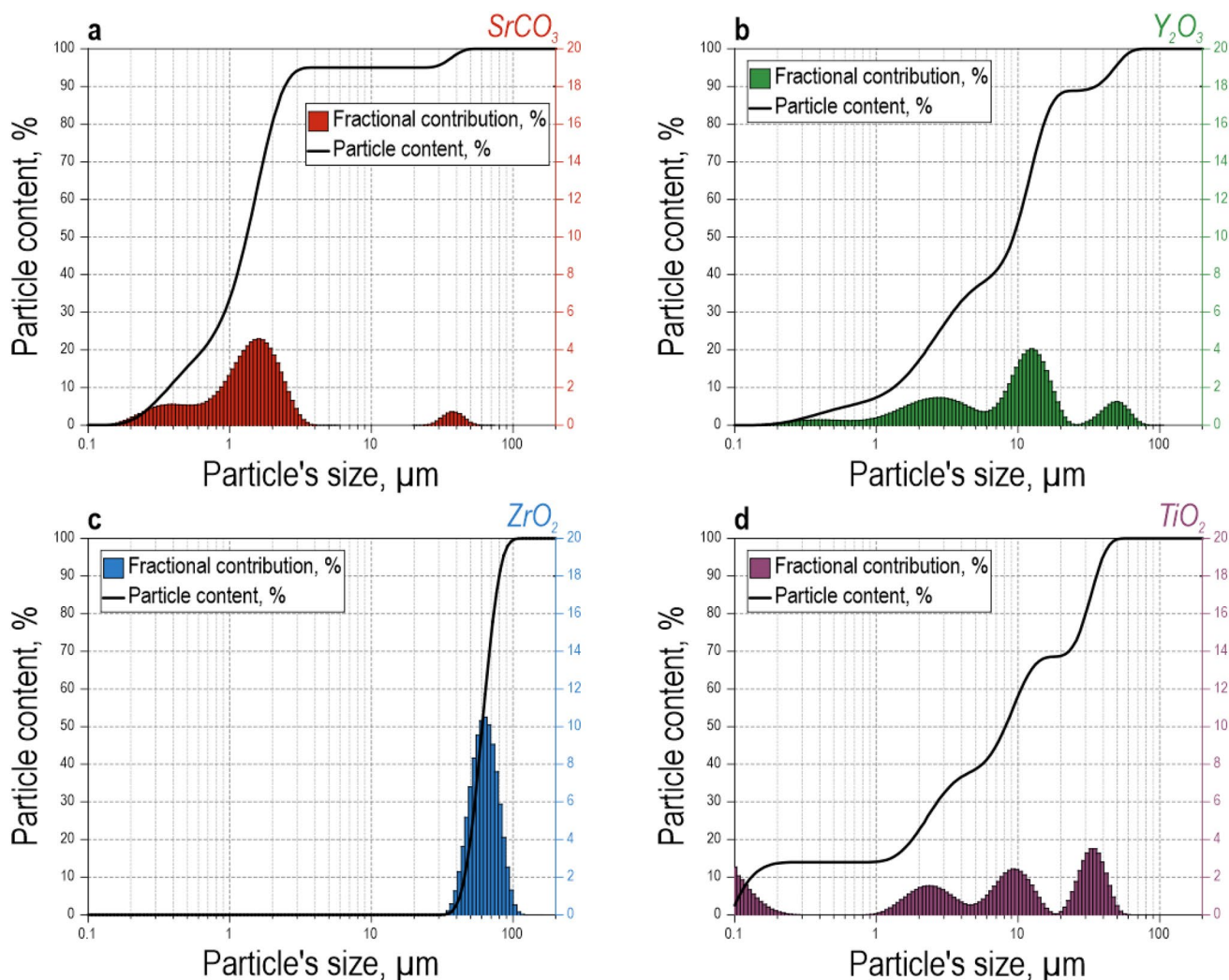
Fig. 2 Granulometric composition (particle size distribution) of initial powders of **a** $SrCO_3$, **b** Y_2O_3, **c** ZrO_2, and **d** TiO_2

(Fig. 4), indicating the absence of a mechanical activation effect on the reactions between substances.

Preparation of ceramic samples and their investigation

### Analysis of reaction mixture sintering kinetics

Based on the SPS-RS results, an analysis of dilatometric curves describing the consolidation kinetics of reaction mixtures was conducted (Fig. 5). The dilatometric curves are divided into sections (Fig. 5) describing specific stages of consolidation.

As seen from Fig. 5, the sintering process occurs in two stages.

Stage 1 describes the initial heating of the powder material and mechanical shrinkage due to the applied uniaxial pressing pressure. At this stage, no significant shrinkage is observed, which is explained by the maximum degree of mechanical arrangement of particles (considering their size from 1 μm and less) and the absence of thermochemical interaction between particles due to their high melting point (Fig. 5a–c).

Stage 2 is characterized by the onset of thermal consolidation. The first signs of thermal consolidation appear at the 6th minute of the process for systems where x = 0.1 and x = 0.2. For systems with higher yttrium and zirconium content (x = 0.3 and x = 1), thermal consolidation begins with a delay—at the 10th minute. This is explained by the composition of the reaction mixtures. At a temperature of about 925 °C, $SrCO_3$ begins to decompose with heat release, causing material shrinkage and initiating reactive interaction of components (Fig. 5a). Systems with higher $SrCO_3$ content (x = 0.1 and x = 0.2) begin to consolidate earlier due to more intense heat release.
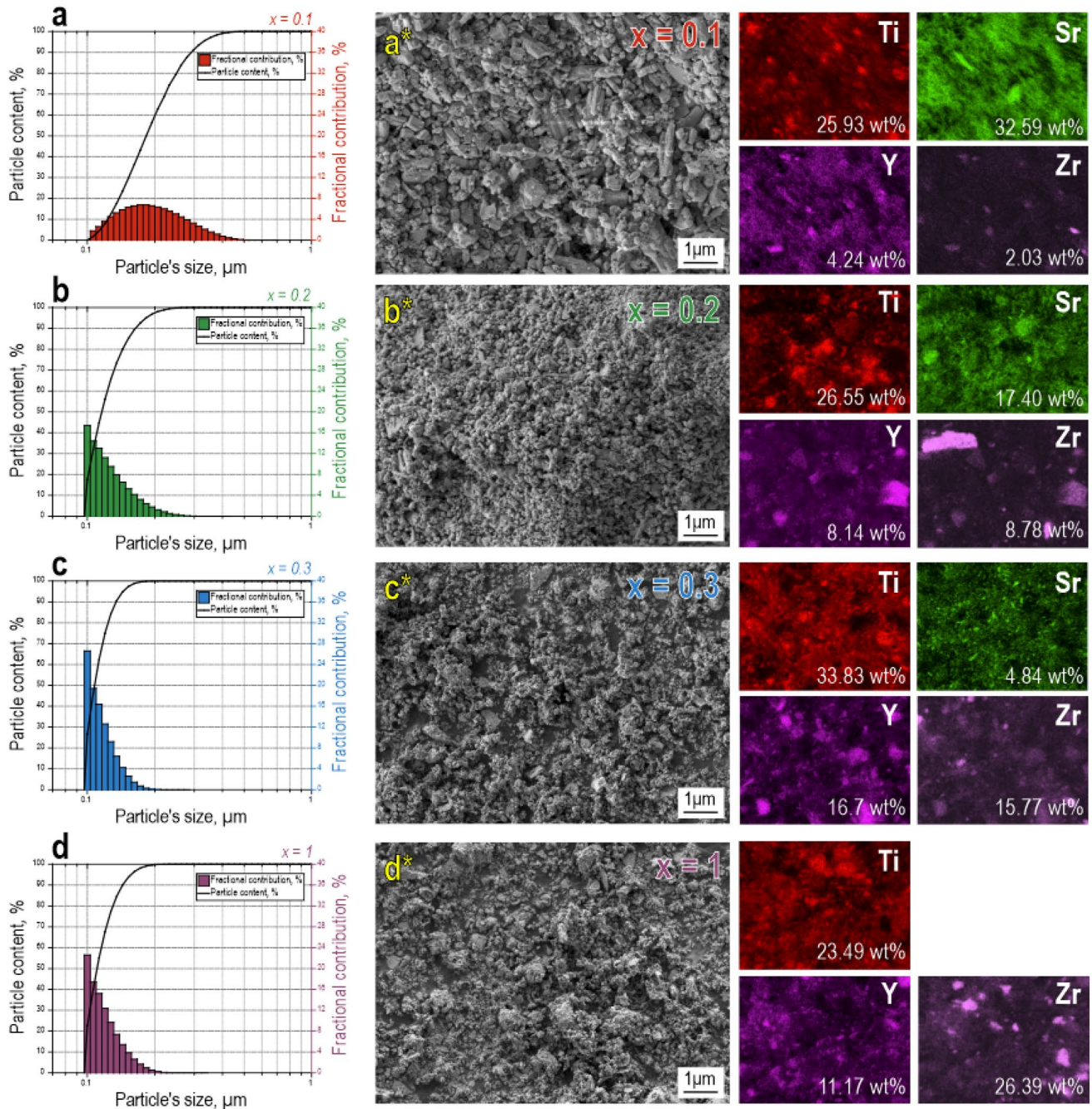
Fig. 3 Granulometric composition of powders of starting reaction mixtures for compositions: **a**, **a*** $Sr_{0.7}Y_{0.1}Zr_{0.1}TiO_3$; **b**, **b*** $Sr_{0.4}Y_{0.2}Zr_{0.2}TiO_3$; **c**, **c*** $Sr_{0.1}Y_{0.3}Zr_{0.3}TiO_3$; and **d**, **d*** $Y_2(Zr_xTi)_2O_7$, obtained by mechanical grinding in a planetary mill (10 min, 870 rpm). **a–d** particle size distribution, **a*–d*** SEM images and EDS element distribution maps

The shrinkage curves reach a plateau for x = 0.1, 0.2, 0.3 and 1 respectively, before reaching the maximum temperature of 1300 °C. This indicates that this temperature is sufficient for complete interaction of the reaction mixture components.

The magnitude of maximum absolute shrinkage tends to decrease from x = 0.1 to x = 1, which is associated with a decrease in $SrCO_3$ content and an increase in the proportion of more refractory components (Y_2O_3 and ZrO_2). The significantly lower shrinkage rate of the x = 1 sample compared to the others is due to the nature of the curve at the initial stage of *Stage 2* (Fig. 5b, c). It lacks sharp changes, indicating a steady and gradual progression of reactions without local overheating and temperature gradients. This consolidation pattern is preferable as it allows for obtaining a more homogeneous material.
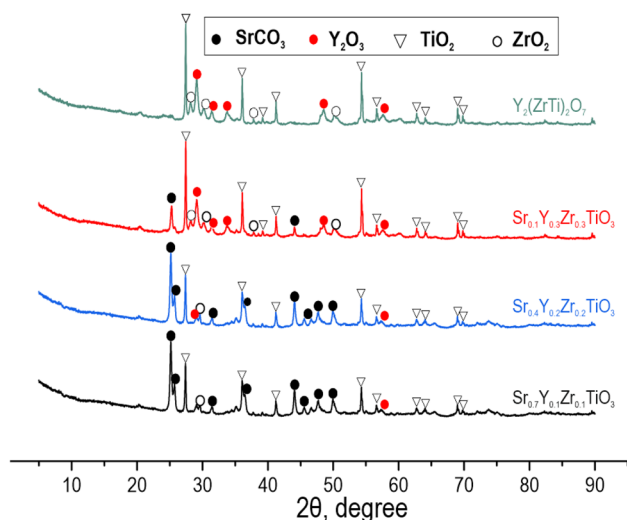
Fig. 4 Phase composition of homogenized reaction mixtures of composition: **a, a*** $Sr_{0.7}Y_{0.1}Zr_{0.1}TiO_3$; **b, b*** $Sr_{0.4}Y_{0.2}Zr_{0.2}TiO_3$; **c, c*** $Sr_{0.1}Y_{0.3}Zr_{0.3}TiO_3$; and **d, d*** $Y_2(Zr_xTi)_2O_7$, obtained by mechanical grinding in a vertical planetary mill (10 min, 870 rpm)

Investigation of phase composition

XRD analysis of the obtained ceramics is presented in Fig. 6. Due to the presence of a large number of components in the reaction mixtures, the XRD is not unambiguously defined, however, the presence of key phases can be identified:

- $SrTiO_3$ with cubic perovskite structure (PDF 89-4934, space group Pm-3 m);
- $Y_2Ti_2O_7$ with cubic pyrochlore structure (PDF 85-1584, space group Fd-3 m);
- $Sr_2(Ti_{0.25}Zr_{0.75})O_4$ with tetragonal structure (PDF 24-1238, space group I4/mmm);
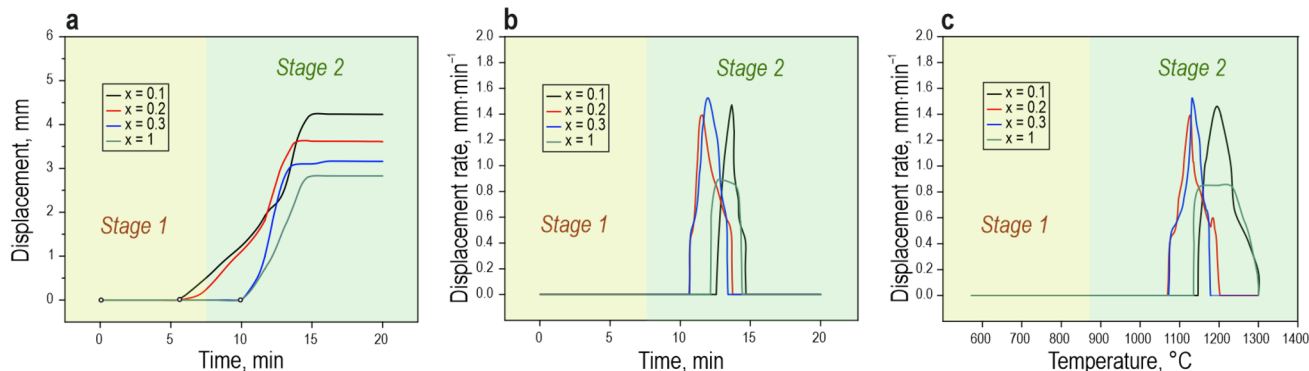
- $Y_2(Zr_{0.6}Ti_{0.4})_2O_{6.99}$ with cubic structure (PDF 83-433, space group Fd-3 m).

With the increase in the ratio from x = 0.1 to x = 1, the number of formed phases also increases. As a result, the ceramic is represented by a complex phase composition, including zirconium and titanate pyrochlore phases (Fig. 6). A noticeable shift of peaks is observed when transitioning from x = 0.2 to x = 0.3 towards a decrease in the diffraction angle, indicating an increase in the crystal lattice due to the formation of a new phase $Y_2(Zr_{0.6}Ti_{0.4})_2O_{6.99}$.

Figure 7 presents a visualization of the structures of $SrTiO_3$, $Y_2Ti_2O_7$, $Sr_2Ti_{0.25}Zr_{0.75}O_7$ using the "VESTA" software package.

For a more comprehensive understanding of phase transformations, an "in situ" X-ray diffraction analysis was conducted using a synchrotron radiation source under heating conditions up to 1000 °C ("in situ" heating synchrotron XRD experiment) for reaction mixtures (Fig. 8), with the component ratios presented in Table 2.

In the case of the $SrCO_3$–TiO_2 mixture (Fig. 8a), it was established that the extinction of the main $SrCO_3$ peaks occurs at approximately 900–950 °C. Within the same temperature range, peaks emerge at around 29 and 34 degrees, reaching their maximum at 950–1000 °C, which should be associated with the orthorhombic → hexagonal transition for $SrCO_3$. Additionally, within this temperature range (circa 850–900 °C), peaks of the final perovskite phase $SrTiO_3$ appear, which is consistent with literature data [37]. It is also indicated that an intermediate phase Sr_2TiO_4 forms. Thus, the study of phase transformation dynamics demonstrates that the formation of $SrTiO_3$ begins as early as 850 °C, although it cannot proceed intensively at this temperature according to literature data [37]. The most prominent peaks of the TiO_2 phase in the anatase structure persist even after some exposure at 1000 °C.

Fig. 5 Sintering kinetics for ceramic samples $Sr_{0.7}Y_{0.1}Zr_{0.1}TiO_3$ (x = 0.1), $Sr_{0.4}Y_{0.2}Zr_{0.2}TiO_3$ (x = 0.2), $Sr_{0.1}Y_{0.3}Zr_{0.3}TiO_3$ (x = 0.3) and $Y_2(Zr_xTi)_2O_7$, describing: **a** absolute shrinkage; **b** shrinkage rate versus time; **c** shrinkage rate versus temperature. Sintering parameters: temperature 1300 °C, holding time 5 min, pressing pressure 21.5 MPa, heating rate 50 °C min^{-1}
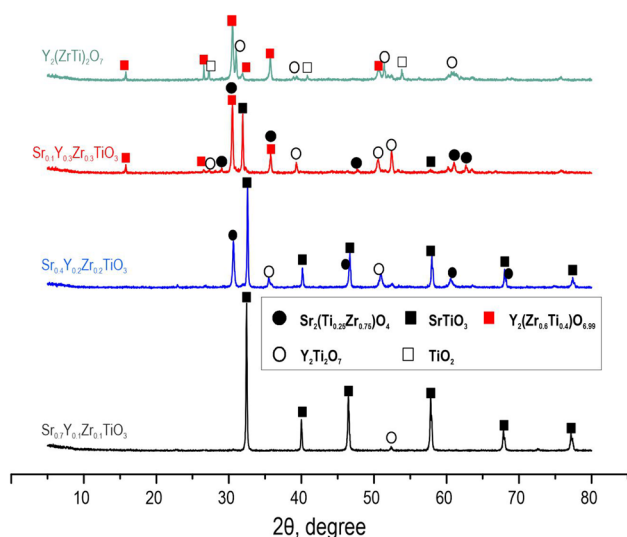
Fig. 6 X-ray diffraction patterns of ceramic samples obtained by SPS-RS technology based on reaction mixtures of the following compositions: $Sr_{0.7}Y_{0.1}Zr_{0.1}TiO_3$ (x = 0.1), $Sr_{0.4}Y_{0.2}Zr_{0.2}TiO_3$ (x = 0.2), $Sr_{0.1}Y_{0.3}Zr_{0.3}TiO_3$ (x = 0.3) and $Y_2(Zr_xTi)_2O_7$ (x = 1)

In the investigation of the Y_2O_3–TiO_2 RM composition (Fig. 8b), it was determined that the pyrochlore phase $Y_2Ti_2O_7$ begins to form at 950 °C. All initial powders also contained TiO_2 phases in anatase and rutile forms, as well as Y_2O_3 phases, which is associated with the incompleteness of the oxide reaction at 1000 °C. As previously demonstrated by XRD analysis, heating the reaction mixture to 1300 °C is optimal, as it achieves a complete chemical reaction of the initial components of the reaction mixture.

The presence of strontium carbonate in the Y_2O_3-$SrCO_3$-TiO_2 RM composition (Fig. 8c) leads to its decomposition with the formation of strontium titanate $SrTiO_3$ at 850–900 °C, along with the formation of the pyrochlore phase $Y_2Ti_2O_7$. Additionally, there is a certain

amount of TiO_2 phases in anatase and rutile forms, as well as Y_2O_3 phases, similar to all studied mixtures.

According to the analysis of the Y_2O_3-TiO_2-ZrO_2 RM composition (Fig. 8d), it is shown that the mixture composition includes TiO_2 phases in anatase and rutile forms, as well as some amount of Y_2O_3 and ZrO_2. It is identified that under the selected parameters of thermal heating up to 1000 °C, reactive sintering with the formation of new phases does not occur. Furthermore, the pyrochlore phase is absent, which is likely due to the high thermal stability of the RM owing to the higher melting point and thermal resistance of ZrO_2 introduced into the mixture, compared to other oxides.

In this regard, it follows that the reactive interaction with the formation of key phases $SrTiO_3$ and $Y_2Ti_2O_7$ is initiated under heating conditions at temperatures of 850–900 °C, in the presence of $SrCO_3$ and Y_2O_3 in the mixture composition. However, in the presence of more thermally stable ZrO_2, the reactive interaction is limited within the capabilities of the in situ XRD analysis method using synchrotron radiation with heating up to 1000 °C. At the same time, laboratory XRD data of the obtained ceramic samples indicate that the pyrochlore phase $Y_2Ti_2O_7$ forms in the composition of ceramics sintered at 1300 °C (Fig. 6), which evidences the occurrence of the reaction at high temperatures. The perovskite phase $SrTiO_3$ is also identified in the composition of ceramic samples (Fig. 6). This indicates that sintering of the specified RM compositions is optimal to be conducted at temperatures above 1000 °C, but not exceeding 1300 °C, under SPS conditions, achieving the required composite composition of mineral-like phases.

Structure analysis

SEM and EDS analyses for the obtained ceramic samples are presented in Fig. 9. The surface morphology of the ceramics is similar. In Fig. 9 *a, a** and *d, d**, ceramic grains are clearly
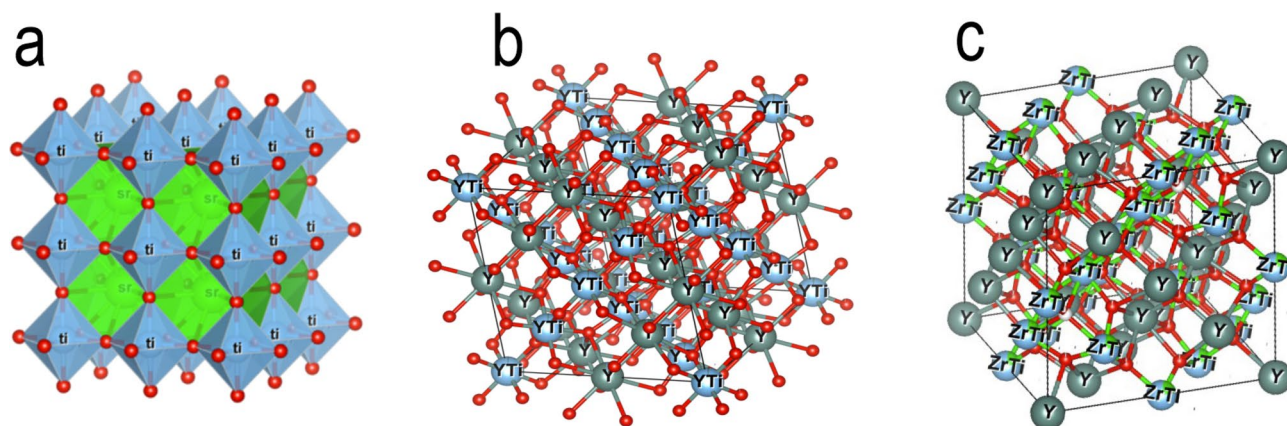
Fig. 7 Visualization of structures (using the "VESTA" software package): **a** $SrTiO_3$; **b** $Y_2Ti_2O_7$; **c** $Sr_2Ti_{0.25}Zr_{0.75}O_7$

Fig. 8 In situ synchrotron X-ray diffraction patterns of the interaction between reaction mixture (RM) components in air: **a** $SrCO_3$–TiO_2; **b** Y_2O_3–TiO_2; **c** Y_2O_3–$SrCO_3$-TiO_2; **d** Y_2O_3–TiO_2–ZrO_2
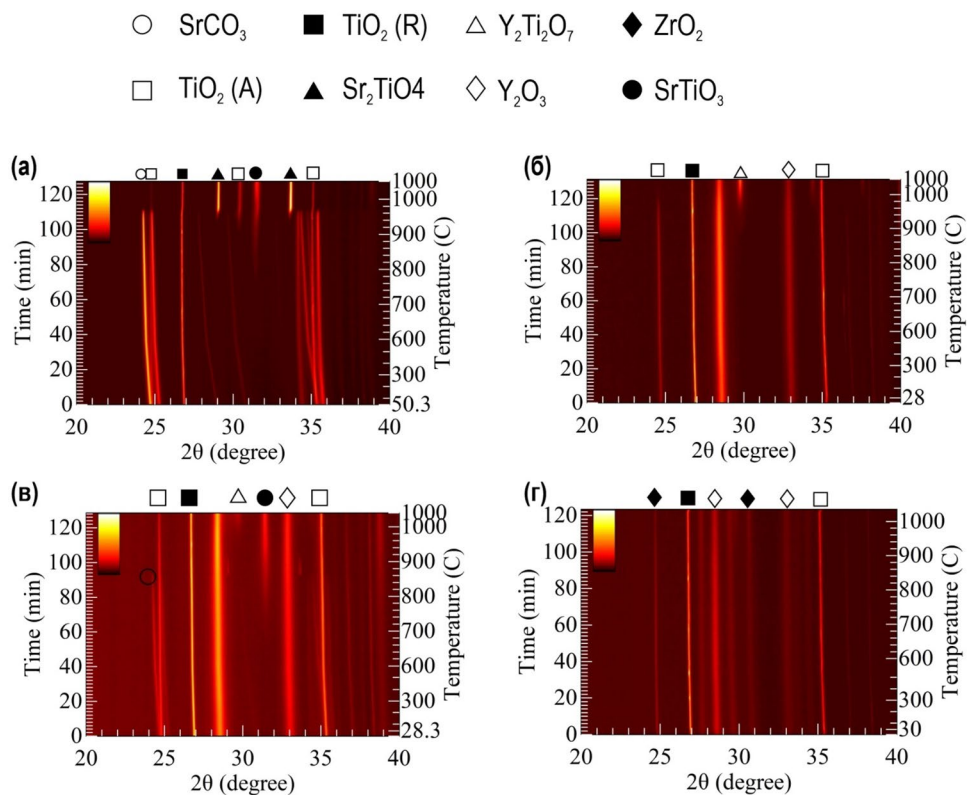
Table 2 Reaction mixture components ratio and their phase composition

Reaction mixture components ratio	$SrCO_3$–TiO_2	Y_2O_3-TiO_2	Y_2O_3-$SrCO_3$-TiO_2	Y_2O_3-TiO_2-ZrO_2
$SrCO_3$	0.65 (1.84)	–	0.1 (1)	–
TiO_2	0.35 (1)	0.51(1.06)	0.4 (4.6)	0.23 (1)
Y_2O_3	–	0.49 (1)	0.5 (5.4)	0.27 (1.08)
ZrO_2	–	–	–	0.5 (2.12)

distinguishable, which is explained, in the case of sample $x = 0.1$, by the monophasic perovskite composition $SrTiO_3$ (perovskite structure—cubic crystal lattice with the structural formula ABO_3); in the case of $x = 1$, by the pyrochlore structure (pyrochlore structure—cubic crystal lattice with the general formula $A_2B_2O_7$). EDS analysis for the sample $x = 0.1$ (Fig. 9a) confirms an almost monophasic composition with uniform element distribution.

In the case of SEM images for samples $x = 0.2$ and $x = 0.3$ (Fig. 9b, b*, c, c*), the formation of monolithic regions at grain boundaries is noticeable, formed from agglomerates, likely of mixed perovskite-pyrochlore composition, which is also shown in XRD (Fig. 6). As the Sr^{2+} content decreases, agglomeration becomes more pronounced. Thus, the change in ceramic composition affects its microstructure—at low Y^{3+} content, the perovskite phase predominates, while with an increase in the Y^{3+} fraction, pyrochlore forms, accompanied by particle agglomeration.

Determination of physical and mechanical characteristics of ceramic samples

For all ceramic samples, specific density and Vickers microhardness were determined (Fig. 10a, b). The sample with $x = 0.2$ possesses the highest density (4.9031 g/cm^3). The sample with $x = 0.1$ has a slightly lower value (4.8247 g/cm^3). The remaining samples show lower density, which is associated with the prevailing phase in the sample composition. It is likely that the density of the perovskite phase $SrTiO_3$ is significantly higher than the presented phases, which is directly related to the composition of the sample $x = 0.1$, as well as the still higher ratio of $SrTiO_3$: $Y_2Ti_2O_7$ phases towards an increase in perovskite. Further decrease in the ratio of the perovskite phase, up to its complete absence, reduces the experimental density to the minimum values among those presented.
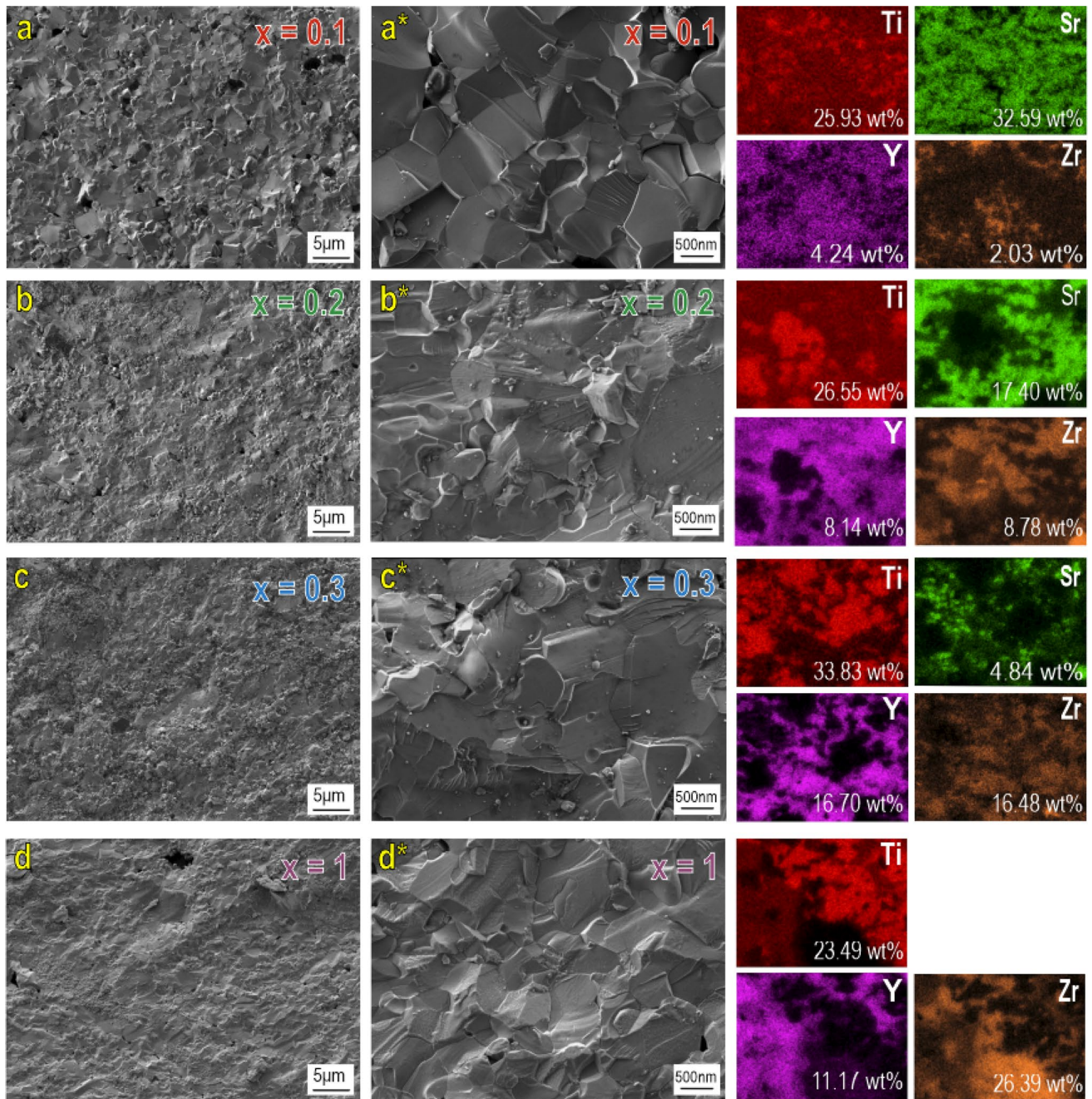
Fig. 9 SEM and EDS images of ceramic samples obtained by R-SPS technology based on reaction mixtures of the following compositions: **a**, **a***
$Sr_{0.7}Y_{0.1}Zr_{0.1}TiO_3$ (x = 0.1); **b**, **b*** $Sr_{0.4}Y_{0.2}Zr_{0.2}TiO_3$ (x = 0.2); **c**, **c*** $Sr_{0.1}Y_{0.3}Zr_{0.3}TiO_3$ (x = 0.3); **d**, **d*** $Y_2(Zr_xTi)_2O_7$ (x = 1)

The box plot (Fig. 10b) presents microhardness (HV) values for four samples with different stoichiometric coefficients of zirconium (x = 0.1, 0.2, 0.3, and 1). For each sample, values are shown with an interquartile range of 25%–75%, median, mean value, and individual experimental points, including statistical outliers. There is a clear trend of increasing microhardness with increasing x value. For the sample with x = 0.1, the mean value is 469 HV. As x increases to 0.2 and 0.3, the microhardness rises to 554 HV

and 690 HV, respectively. The sample with x = 1 exhibits the maximum microhardness with a mean value of about 656 HV. The increase in the Zr^{4+} fraction positively affects the achieved microhardness level, which may be related to the higher hardness of the pyrochlore phase compared to the perovskite phase.

Analysis of interquartile ranges shows the narrowest distribution for the sample x = 0.2, which is consistent with SEM results (Fig. 9b, b*) demonstrating a more

Fig. 10 Physical and mechanical characteristics of ceramic samples obtained by SPS-RS technology based on reaction mixtures of the following compositions: $Sr_{0.7}Y_{0.1}Zr_{0.1}TiO_3$ (x = 0,1), $Sr_{0.4}Y_{0.2}Zr_{0.2}TiO_3$ (x = 0,2), $Sr_{0.1}Y_{0.3}Zr_{0.3}TiO_3$ (x = 0,3) and $Y_2(Zr_xTi)_2O_7$: (a) density and (b) microhardness
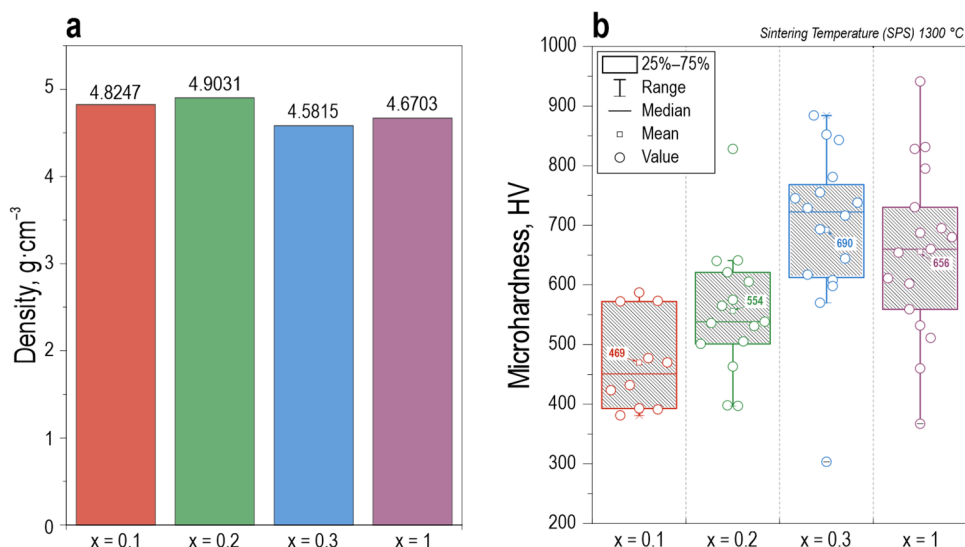
homogeneous microstructure of this sample. Asymmetry in microhardness distribution is observed for some compositions. Positive asymmetry, where the median is lower than the mean (x = 0.1 and 0.2), indicates the presence of outliers with high hardness values. Negative asymmetry for x = 0.3 (median higher than mean) suggests a concentration of data values in the high hardness region. For x = 1, asymmetry is practically absent, as evidenced by the median line lying at the level of the mean value. Statistical outliers are present for samples x = 0.2 and 0.3, indicating structural inhomogeneity of these materials.

Thus, analysis of the microhardness box plot in conjunction with microstructural data indicates a more complex phase composition of ceramics with increasing Zr^{4+} content, leading to structural and property inhomogeneity.

Evaluation of hydrolytic stability of ceramic samples

To study leaching mechanisms, calculations of the following parameters were performed: total leaching fraction, leaching depth, and effective diffusion coefficient. Data on the hydrolytic stability of matrices with respect to strontium are presented in Fig. 11 and Table 3.

The hydrolytic stability values of the obtained ceramic samples on the 30th day of exposure are satisfactory and range from 10^{-5} to 10^{-7} g cm^{-2}•day for all studied compositions (Fig. 11a). These values indicate high resistance of the synthesized materials to leaching under the given conditions.

Analysis of strontium leaching kinetics (Fig. 11b) reveals a change in the process mechanism over time. For the sample with x = 0.1, in the initial stage up to 3 days, the tangent of the slope angle of the total leaching fraction dependence on the logarithm of time is 0.8456, indicating the predominance
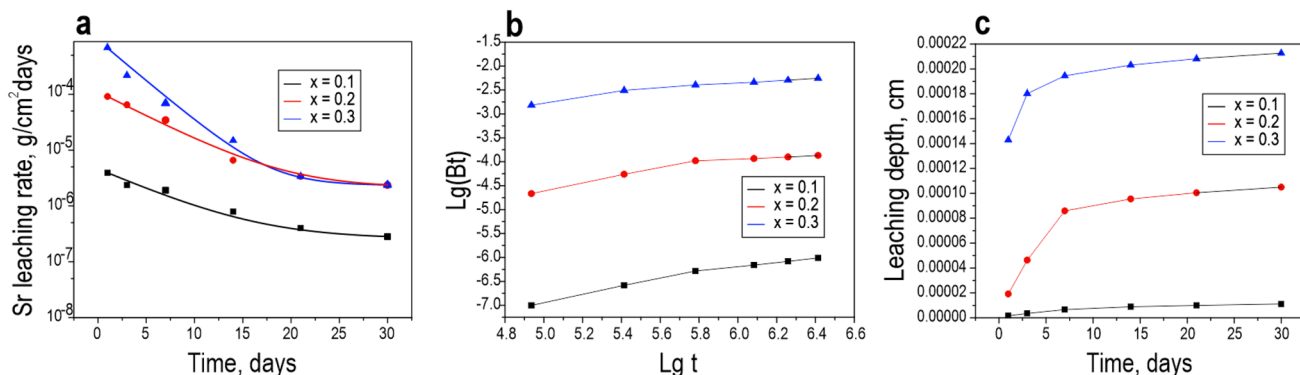
Fig. 11 Hydrolytic stability of ceramic samples obtained by R-SPS technology based on reaction mixtures of compositions $Sr_{0.7}Y_{0.1}Zr_{0.1}TiO_3$ (x = 0.1), $Sr_{0.4}Y_{0.2}Zr_{0.2}TiO_3$ (x = 0.2), $Sr_{0.1}Y_{0.3}Zr_{0.3}TiO_3$ (x = 0.3), $Y_2(Zr_xTi)_2O_7$ (x = 1): (a) Sr^{2+} leaching rate from the ceramic volume; (b) dependence of the logarithm of the leached fraction of Sr^{2+} from ceramics on the logarithm of leaching time; (c) dependence of leaching depth on time

of the surface layer dissolution mechanism. After 3 days, the tangent of the angle decreases to 0.4354, indicating a transition to a diffusion mechanism of strontium transfer from the matrix volume. The high initial leaching rate may be associated with the presence of a near-surface layer of adsorbed strontium, which is predominantly leached at an early stage. The presence of a break in the kinetic curve suggests that part of the strontium is not structured in the material volume.

For samples x = 0.2 and 0.3, the leaching kinetics are similar, but the transition between mechanisms is observed on the 7th day. Considering the decrease in the $SrTiO_3$ phase fraction in these compositions compared to x = 0.1, it can be assumed that the delay in transition is associated with the formation of sparingly soluble phases on the surface that do not contain strontium, such as yttrium pyrochlore.

The leachability index (L) is a value characterizing the rate of radionuclide release from the material upon contact with an aqueous medium. For all studied compositions, L

values exceed 8, which meets the requirements for radioactive waste immobilization matrices [38].

The calculated values of the leaching front penetration depth (Fig. 11c) indicate high stability of ceramic matrices due to their dense structure and chemical inertness. However, samples with lower strontium content show greater leaching depth, which may be associated with the presence of soluble strontium-containing phases on the surface of these materials.

For yttrium-containing samples, the hydrolytic stability value stabilizes on the 15th day and ranges from 10^{-4} to 10^{-5} g cm^{-2}•day for all compositions (Fig. 12a, Table 4). The tangent of the slope angle of the curves of the total leaching fraction dependence on the logarithm of time (Fig. 12b) remains constant (0.5532), indicating a diffusion mechanism of yttrium leaching from the material volume. The leaching front penetration depth (Fig. 12c) decreases with increasing Y^{3+} content, which may be

Table 3 Strontium leaching parameters on the 30th day

Sample	Diffusion coefficient, D_e, cm^2/s	Error, cm^2/s	L	Error	Depth, cm	Error, cm
$(Sr_{0.7}Y_{0.1}Zr_{0.1}TiO_3)$	1.54×10^{-12}	$\pm 0.070 \times 10^{-12}$	11.81	± 0.5905	1.10×10^{-5}	$\pm 0.055 \times 10^{-5}$
$(Sr_{0.4}Y_{0.2}Zr_{0.2}TiO_3)$	5.30×10^{-11}	$\pm 0.265 \times 10^{-11}$	10.28	± 0.514	1.05×10^{-4}	$\pm 0.052 \times 10^{-4}$
$(Sr_{0.1}Y_{0.3}Zr_{0.3}TiO_3)$	4.38×10^{-10}	$\pm 0.219 \times 10^{-10}$	9.36	± 0.468	2.13×10^{-4}	$\pm 0.106 \times 10^{-4}$
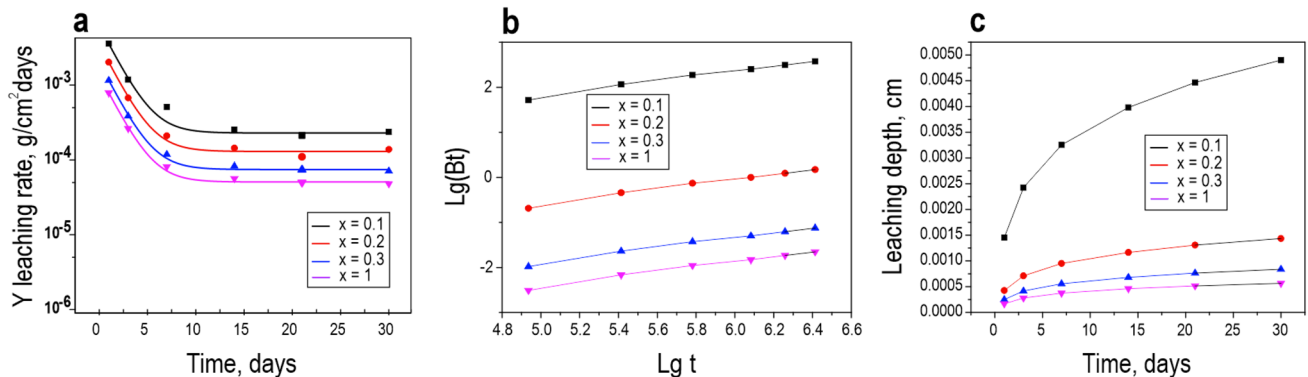
Fig. 12 Hydrolytic stability of ceramic samples obtained by R-SPS technology based on reaction mixtures of compositions $Sr_{0.7}Y_{0.1}Zr_{0.1}TiO_3$ (x=0.1), $Sr_{0.4}Y_{0.2}Zr_{0.2}TiO_3$ (x=0.2), $Sr_{0.1}Y_{0.3}Zr_{0.3}TiO_3$ (x=0.3), $Y_2(Zr_xTi)_2O_7$ (x=1): (a) Y^{3+} leaching rate from the ceramic volume; (b) dependence of the logarithm of the leached fraction of Y^{3+} from ceramics on the logarithm of leaching time; (c) dependence of leaching depth on time

Table 4 Y^{3+} leaching parameters on the 30th day

Sample	Diffusion coefficient, D_e, cm^2/s	Error, cm^2/s	L	Error	Depth, cm	Error, cm
$(Sr_{0.7}Y_{0.1}Zr_{0.1}TiO_3)$	5.12×10^{-5}	$\pm 0.256 \times 10^{-5}$	4.29	± 0.214	4.90×10^{-3}	$\pm 0.245 \times 10^{-3}$
$(Sr_{0.4}Y_{0.2}Zr_{0.2}TiO_3)$	6.92×10^{-7}	$\pm 0.346 \times 10^{-7}$	6.16	± 0.308	1.43×10^{-3}	$\pm 0.071 \times 10^{-3}$
$Sr_{0.1}Y_{0.3}Zr_{0.3}TiO_3)$	5.00×10^{-8}	$\pm 0.250 \times 10^{-8}$	7.30	± 0.365	8.39×10^{-4}	$\pm 0.419 \times 10^{-4}$
$Y_2(Zr_xTi)_2O_7$	2.80×10^{-8}	$\pm 0.140 \times 10^{-8}$	7.55	± 0.377	5.65×10^{-4}	$\pm 0.282 \times 10^{-4}$

associated with the stabilization of the crystal structure of the matrices.

Similarly to yttrium, the hydrolytic stability with respect to Zr^{4+} stabilizes on the 14th day in the range from 10^{-4} to 10^{-5} g cm^{-2}•day (Fig. 13a, Table 5). The tangent angle value of 0.5532 (Fig. 13b) indicates a diffusion leaching mechanism. The Zr^{4+} leaching depth curves (Fig. 13c) are practically identical to those for Y^{3+} (Fig. 12c), suggesting that these elements are located in the same crystalline phase, for example, with a pyrochlore structure. The curves in Fig. 13b are essentially identical to those in Fig. 12b. Thus, Zr^{4+} and Y^{3+} should be in the same phase, which is confirmed by the results of X-ray phase analysis (Fig. 6). To the same extent, the curves for Zr^{4+} correspond to the curves for Sr^{2+} (Fig. 11).

Considering the obtained results, it can be asserted that the identified peaks of the co-location of $Sr_2Ti_{0.25}Zr_{0.75}O_7$ and $Y_2(Zr_{0.6}Ti_{0.4})O_{6.99}$ in the diffractograms (Fig. 6) correspond to the second phase.

The use of reactive SPS-RS technology ensured the production of ceramic compositions with high density due to the intensification of diffusion processes during consolidation. At the specified temperature, stable ceramic matrices of complex composition were obtained, the properties of which undergo changes depending on the ratio of the initial components.

A detailed study of the physicochemical and mechanical characteristics of the obtained ceramics demonstrated their high quality. In addition to high density, the materials possess microhardness up to 950 HV and a homogeneous, non-porous microstructure.

Furthermore, a key result of the work was the achievement of hydrolytic stability of the obtained ceramic matrices with respect to the leaching of Sr^{2+}, Y^{3+}, and Zr^{4+} ions, which is 10^{-5}–10^{-7} g cm^{-2}·day, satisfying the parameters of GOST R 50926-96. The leachability index value is above 8, indicating the formation of strong chemical bonds of radionuclides in the crystal structures of the matrices [38]. Thus, the proposed approach demonstrates promise for obtaining ceramics with high potential reliability for long-term immobilization of radionuclides.

Conclusion

This study implemented solid-phase synthesis of mineral-like composite ceramics based on $SrTiO_3$, $Y_2Ti_2O_7$, $Y_2(Zr_{0.6}Ti_{0.4})_2O_{6.99}$ and $Sr_2Ti_{0.25}Zr_{0.75}O_7$, promising for the immobilization of radionuclides ^{90}Sr and ^{90}Y, as well as the ^{90}Zr isotope, as a decay product in the chain $^{90}Sr \rightarrow {}^{90}Y \rightarrow {}^{90}Zr$. The sintering kinetics of the reaction mixture with stoichiometric formulas $Sr_{1-3x}Y_xZr_xTiO_3$ and
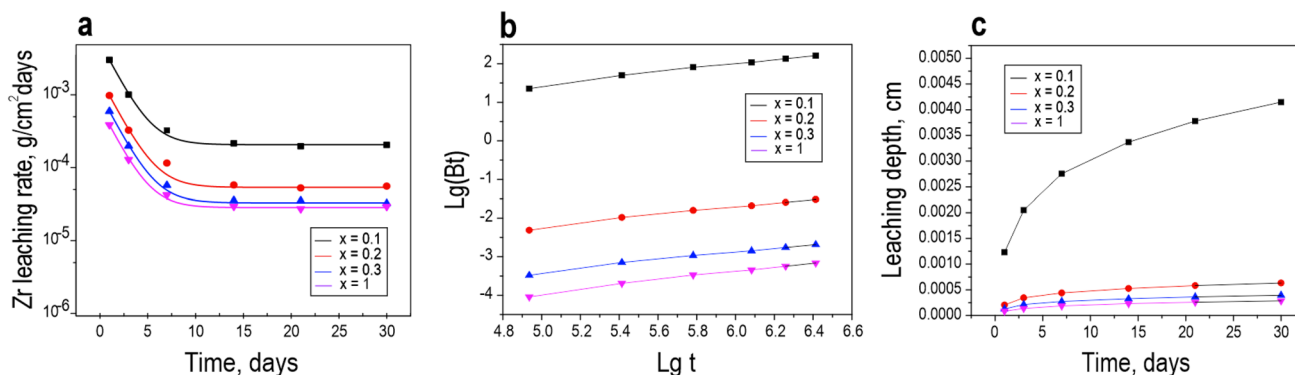
Fig. 13 Hydrolytic stability of ceramic samples obtained by SPS-RS technology based on reaction mixtures of compositions $Sr_{0.7}Y_{0.1}Zr_{0.1}TiO_3$ (x=0.1), $Sr_{0.4}Y_{0.2}Zr_{0.2}TiO_3$ (x=0.2), $Sr_{0.1}Y_{0.3}Zr_{0.3}TiO_3$ (x=0.3), $Y_2(Zr_xTi)_2O_7$ (x=1): (a) Zr^{4+} leaching rate from the ceramic volume; (b) dependence of the logarithm of the leached fraction of Zr^{4+} from ceramics on the logarithm of leaching time; (c) dependence of leaching depth on time

Table 5 Zr^{4+} leaching parameters on the 30th day

Sample	Diffusion coefficient, D_e, cm^2/s	Error, cm^2/s	L	Error	Depth, cm	Error, cm
$Sr_{0.7}Y_{0.1}Zr_{0.1}TiO_3$	2.63×10^{-5}	$\pm 0.131 \times 10^{-5}$	4.58	± 0.229	4.15×10^{-3}	$\pm 0.207 \times 10^{-3}$
$Sr_{0.4}Y_{0.2}Zr_{0.2}TiO_3$	2.60×10^{-8}	$\pm 0.130 \times 10^{-8}$	7.58	± 0.379	6.34×10^{-4}	$\pm 0.317 \times 10^{-4}$
$Sr_{0.1}Y_{0.3}Zr_{0.3}TiO_3$	2.41×10^{-9}	$\pm 0.120 \times 10^{-9}$	8.62	± 0.431	3.94×10^{-4}	$\pm 0.197 \times 10^{-4}$
$Y_2(Zr_xTi)_2O_7$	1.84×10^{-9}	$\pm 0.092 \times 10^{-9}$	8.74	± 0.437	2.86×10^{-4}	$\pm 0.143 \times 10^{-4}$

$Y_2(Zr_xTi)_2O_7$ was investigated, as well as structural-phase changes of the resulting ceramics under spark plasma sintering conditions using XRD, SEM, EDS methods, and XRD at a synchrotron radiation source under "in situ" heating conditions ("in situ" heating synchrotron XRD experiment).

The study of the densification dynamics of the reaction mixture for the specified compositions was conducted at a constant temperature of 1300 °C and pressure of 21.5 MPa, where it was shown that the "in situ" reaction interaction and simultaneous sintering of the initial powder mixture proceeds through two stages of compaction: Stage 1—mechanical shrinkage due to applied pressure, during which no significant shrinkage is observed; Stage 2—thermal consolidation, the start time of which varies depending on the composition of the reaction mixture. The plateauing of the curves identifies the complete reaction interaction of the system components.

According to "in situ" XRD analysis data on synchrotron radiation, it was established that the reaction interaction with the formation of $SrTiO_3$ and $Y_2Ti_2O_7$ phases is initiated under heating conditions at temperatures of 850–900 °C, in the presence of $SrCO_3$ and Y_2O_3 in the mixture composition. However, in the presence of more thermally stable ZrO_2, the reaction interaction is limited to 1000 °C, and only heating at a higher temperature up to 1300 °C initiates the formation of the required perovskite and pyrochlore phases in the ceramic composition.

The obtained ceramic samples are characterized by high density up to 4.9 g cm^{-3}, non-porous microstructure, and microhardness up to 950 HV. The variation of these characteristics depends on the composition and structure of the ceramics, in particular, the decrease in sample density is due to the increase in the content of the $Y_2Ti_2O_7$ phase, which has a lower theoretical density than $SrTiO_3$. At the same time, increasing the Zr fraction in the ceramic composition leads to an increase in the microhardness of the samples, up to maximum values at $x=1$, and statistical selections on the box plots indicate structural inhomogeneity.

It has been proven that this ceramic possesses high hydrolytic stability, as the leaching rate of Sr^{2+} reaches 10^{-7} g cm^{-2} day, and for Y^{3+} and Zr^{4+} 10^{-5} g cm^{-2} day, which meets the requirements of GOST R 50926-96 and ANSI/ANS 16.1 for solidified high-level waste in relation to Sr^{2+}. The leaching mechanism of these ions from the ceramic volume has been established, indicating diffusion leaching with minimal diffusion depth of ions from the volume to the ceramic surface. This is due to the effective binding of radionuclides ^{90}Sr, ^{90}Y, and the stable isotope ^{90}Zr, in the crystal structures of perovskite and pyrochlore.

The perovskite phase $SrTiO_3$ provides reliable immobilization of ^{90}Sr through isomorphic substitution of Ca^{2+} cations in the $CaTiO_3$ structure, while pyrochlores $Y_2Ti_2O_7$ and $Y_2(Zr_{0.6}Ti_{0.4})_2O_{6.99}$ provide immobilization of ^{90}Y through isomorphic substitution of Ca^{2+} and Na in the $(NaCa)_2Nb_2O_7$ structure, and ^{90}Zr, respectively, through isomorphic substitution of Nb^{3+} cations. A comprehensive study has shown the promise of the developed ceramic matrices for reliable long-term immobilization of the specified radionuclides.

Declarations

Conflict of interest The authors declare that they have no known competing financial interests or personal relationships that could have appeared to influence the work reported in this paper. The authors declare the following financial interests/personal relationships which may be considered as potential competing interests:

References

1. Kvashnina K, Claret F, Clavier N, Levitskaia TG, Wainwright H, Yao T (2024) Long-term, sustainable solutions to radioactive waste management. Sci Rep 14:5907. https://doi.org/10.1038/s41598-024-55911-y

2. Evans C, Gabriel S, Polak C, Valbuena P (2024) The costs of nuclear fuel, In: Nucl Econ 1, Wiley, pp 163–233. https://doi.org/10.1002/9781394257348.ch4

3. Kumar P, Yadav S, Yadav A (2024) Radioactive waste minimization and management. In: Green Chem Approaches to Environ Sustain, Elsevier, pp 165–184. https://doi.org/10.1016/B978-0-443-18959-3.00003-3

4. Okamoto J, Fujita T, Hara K, Sasaki N (1991) Effect of heat from high-level waste on performance of deep geological repository. In: Manag. Radioact. Wastes, Non-Radioactive Wastes from Nucl Facil, pp 1034–1040

5. Kim G-Y, Shin S-S, Lee B, Choi J-H, Kang HW, Pyo J-Y, Yang JH, Park H-S, Lee KR (2024) Characteristics of Cs pollucite synthesized at various Cs loadings for immobilization of radioactive Cs. J Nucl Mater 588:154781. https://doi.org/10.1016/j.jnucmat.2023.154781

6. Shichalin OO, Papynov EK, Ivanov NP, Balanov MI, Drankov AN, Shkuratov AL, Zarubina NV, Fedorets AN, Mayorov VY, Lembikov AO, Shi Y, Tananaev IG, Ivanets AI (2023) Study of adsorption and immobilization of Cs^+, Sr^{2+}, Co^{2+}, Pb^{2+}, La^{3+} ions on Na-faujasite zeolite transformed in solid state matrices. Sep Purif Technol 332:125662. https://doi.org/10.1016/j.seppur.2023.125662

7. Panasenko AE, Shichalin OO, Yarusova SB, Ivanets AI, Belov AA, Drankov AN, Azon SA, Fedorets AN, Buravlev IY, Mayorov

VY, Shlyk DK, Buravleva AA, Merkulov EB, Zarubina NV, Papynov EK (2022) A novel approach for rice straw agricultural waste utilization: synthesis of solid aluminosilicate matrices for cesium immobilization. Nucl Eng Technol 54:3250–3259. https://doi.org/10.1016/j.net.2022.04.005

8. Sayenko SY, Shkuropatenko VA, Pylypenko OV, Karsim SO, Zykova AV, Kutnii DV, Wagh AS (2022) Radioactive waste immobilization of Hanford sludge in magnesium potassium phosphate ceramic forms. Prog Nucl Energy 152:104315. https://doi.org/10.1016/j.pnucene.2022.104315

9. Rykunova AA, Kashcheev VA, Shadrin AY, Shmidt OV (2023) Calculation algorithm of volumes of medium-level radioactive wastes solidified into cement or magnesium-potassium phosphate (MPP) matrix. Theor Found Chem Eng 57:725–731. https://doi.org/10.1134/S0040579523040243

10. Ivanets A, Shashkova I, Kitikova N, Radkevich A, Venhlinskaya E, Dzikaya A, Trukhanov AV, Sillanpää M (2021) Facile synthesis of calcium magnesium zirconium phosphate adsorbents transformed into $MZr_4P_6O_{24}$ (M: Ca, Mg) ceramic matrix for radionuclides immobilization. Sep Purif Technol 272:118912. https://doi.org/10.1016/j.seppur.2021.118912

11. Liu H, Wang H, Zhao J, Li J, Zhang X, Yang J, Zhu Y, Xie R, Zheng K, Huang H, Huo J (2022) Immobilization of Cs and Sr within perovskite-type Ba0.7-ySry(La, Cs)0.3ZrO3 glass/ceramic composite waste forms. Ceram. Int. 48:34298–34307. https://doi.org/10.1016/J.CERAMINT.2022.08.007

12. Bensemma N, Moudir D, Ararem A, Sari A, Maachou A (2023) Synthesis, phase stability and chemical leaching behavior of Nd-doped $CaTiO_3$ perovskite ceramics for radioactive waste immobilization. J Aust Ceram Soc 59:923–934. https://doi.org/10.1007/s41779-023-00885-9

13. Reiser JT, Tolman KR, Kropp MT, Kissinger RM, Saslow SA, Cutforth DA, Crum JV, Seiner BN, Smith GL, Vienna JD (2022) Fabrication of radioactive and non-radioactive titanate and zirconate ceramics for immobilization of used nuclear fuel. J Nucl Mater 572:154033. https://doi.org/10.1016/j.jnucmat.2022.154033

14. Li L, Xu Z, Li H, Li J, Hu D, Xiang Y, Han L, Peng X (2022) Immobilization of strontium and cesium by aluminosilicate ceramics derived from metakaolin geopolymer-zeolite a composites via 1100 °C heating treatment. Ceram Int 48:15236–15242. https://doi.org/10.1016/J.CERAMINT.2022.02.054

15. Luo J, Li X, Zhang F, Chen S, Ren D (2021) Sintering of monoclinic $SrAl_2Si_2O_8$ ceramics and their Sr immobilization. Int J Miner Metall Mater 28:1057–1062. https://doi.org/10.1007/s12613-020-2056-6

16. Papynov EK, Shichalin OO, Belov AA, Buravlev IY, Portnyagin AS, Azon SA, Shlyk DK, Buravleva AA, Parot'kina YA, Nepomnyushchaya VA, Kornakova ZE, Gridasov AV, Tananaev IG, Sergienko VI (2021) Synthesis of mineral-like $SrWO_4$ ceramics with the scheelite structure and a radioisotope product based on it. Russ. J. Inorg. Chem. 66:1434–1446. https://doi.org/10.1134/S0036023621090114

17. Shichalin OO, Belov AA, Zavyalov AP, Papynov EK, Azon SA, Fedorets AN, Buravlev IY, Balanov MI, Tananaev IG, Shi Y, Zhang Q, Niu M, Liu W, Portnyagin AS (2022) Reaction synthesis of $SrTiO_3$ mineral-like ceramics for strontium-90 immobilization via additional in-situ synchrotron studies. Ceram Int 48:19597–19605. https://doi.org/10.1016/j.ceramint.2022.03.068

18. Sun S, Bailey DJ, Gardner LJ, Hyatt NC (2022) Ceramic-based stabilization / solidification of radioactive waste. Inc. https://doi.org/10.1016/B978-0-12-824004-5.00021-9

19. Zhao J, Li J, Liu H, Zhang X, Zheng K, Yu H, Lian Q, Wang H, Zhu Y, Huo J (2020) Cesium immobilization in perovskite-type Ba1-x(La, Cs)xZrO3 ceramics by sol-gel method. Ceram Int 46:9968–9971. https://doi.org/10.1016/j.ceramint.2019.12.219

20. Chen P, Tian T, Zhang C, Tang X, Li Z (2023) Effect of Ce-doping on the phase composition and aqueous stability of $Gd_2Hf_2O_7$ ceramic as nuclear waste forms. Ceram Int 49:38556–38565. https://doi.org/10.1016/j.ceramint.2023.09.188

21. Rawat D, Govind B (2023) Exploring the influence of lanthanides on the structure and thermodynamic stability of $SrLnTh(PO_4)_3$ (Ln = La, Nd, Sm, Eu, and Gd). J Therm Anal Calorim 148:12071–12081. https://doi.org/10.1007/s10973-023-12532-3

22. Zuo S, Lu Y, Lu X, You Y, Shu X, Chen J (2023) Free occupying mechanism of simulated tetravalent waste ions in $Gd_2Zr_2O_7$ and performance evaluation of the waste forms. J Am Ceram Soc 106:7088–7097. https://doi.org/10.1111/jace.19303

23. Bensemma N, Moudir D, Ararem A, Sari A, Maachou A (2023) Synthesis, phase stability and chemical leaching behavior of Nd—doped—$CaTiO_3$ perovskite ceramics for radioactive waste immobilization. J Aust Ceram Soc 59:923–934. https://doi.org/10.1007/s41779-023-00885-9

24. Papynov EK, Shichalin OO, Belov AA, Buravlev IY, Zavjalov A, Azon SA, Fedorets AN, Kornakova ZE, Lembikov AO, Gridasova EA, Ivanets A, Tananaev IG (2023) Perovskite/pyrochlore composite mineral-like ceramic fabrication for $^{90}Sr/^{90}Y$ immobilization using SPS-RS technique. Coatings 13:2027. https://doi.org/10.3390/coatings13122027

25. Bhuiyan A, Wong V, Abraham JL, Aughterson RD, Kong L, Farzana R, Gregg DJ, Sorrell CC, Zhang Y, Koshy P (2021) Phase assemblage and microstructures of $Gd_2Ti_2-xZrxO_7$ (x = 0.1–0.3) pyrochlore glass-ceramics as potential waste forms for actinide immobilization. Mater. Chem. Phys. 273:125058. https://doi.org/10.1016/j.matchemphys.2021.125058

26. Zhao Z, Hu P, Yang Y, Wang L, Xie H, Yin W, Liu J, Ding Y (2023) Hot pressing preparation of $Y_2Ti_2O_7$-based glass-ceramics as potential waste forms for actinide immobilization. Ceram Int 49:2515–2521. https://doi.org/10.1016/j.ceramint.2022.09.227

27. Xie H, Lan R, Wang L, Ding Y (2023) Preparation and chemical stability evaluation of new (Nd, An)$_2$Zr$_2$O$_7$-SrZrO$_3$ multiphase ceramics. J Aust Ceram Soc 59:751–761. https://doi.org/10.1007/s41779-023-00871-1

28. Dran'kov A, Shichalin O, Papynov E, Nomerovskii A, Mayorov V, Pechnikov V, Ivanets A, Buravlev I, Yarusova S, Zavjalov A, Ognev A, Balybina V, Lembikov A, Tananaev I, Shapkin N (2022) Hydrothermal synthesis, structure and sorption performance to cesium and strontium ions of nanostructured magnetic zeolite composites. Nucl. Eng. Technol. 54:1991–2003. https://doi.org/10.1016/j.net.2021.12.010

29. Zhushchikhovskaya IS, Buravlev IY (2021) Ancient ceramic casting molds from the Southern Russian Far East: identification of alloy traces via application of nondestructive SEM-EDS and pXRF Methods. Heritage 4:2643–2667. https://doi.org/10.3390/heritage4040149

30. Buravlev IY, Gelman EI, Lapo EG, Pimenov VA, Martynenko AV (2022) Three-colored Sancai glazed ceramics excavated from Bohai sites in Primorye (Russia). J Archaeol Sci Rep 41:103346. https://doi.org/10.1016/j.jasrep.2022.103346

31. Papynov EK, Shichalin OO, Buravlev IY, Belov AA, Portnyagin AS, Fedorets AN, Azarova YA, Tananaev IG, Sergienko VI (2020) Spark plasma sintering-reactive synthesis of $SrWO_4$ ceramic matrices for ^{90}Sr immobilization. Vacuum 180:109628. https://doi.org/10.1016/j.vacuum.2020.109628

32. Momma K, Izumi F (2011) VESTA 3 for three-dimensional visualization of crystal, volumetric and morphology data. J Appl Crystallogr 44:1272–1276. https://doi.org/10.1107/S0021889811038970

33. Evdokov OV, Titov VM, Tolochko BP, Sharafutdinov MR (2009) In situ time-resolved diffractometry at SSTRC. Nuclear Instrum Methods Phys Res Sect A Accel Spectrom Detect Assoc Equip 603:194–195. https://doi.org/10.1016/j.nima.2009.03.001

34. Piminov PA, Baranov GN, Bogomyagkov AV, Berkaev DE, Borin VM, Dorokhov VL, Karnaev SE, Kiselev VA, Levichev EB, Meshkov OI, Mishnev SI, Nikitin SA, Nikolaev IB, Sinyatkin SV, Vobly PD, Zolotarev KV, Zhuravlev AN (2016) Synchrotron radiation research and application at VEPP-4. Phys Procedia 84:19–26. https://doi.org/10.1016/j.phpro.2016.11.005

35. Aulchenko VM, Evdokov OV, Kutovenko VD, Pirogov BY, Sharafutdinov MR, Titov VM, Tolochko BP, Vasiljev AV, Zhogin IA, Zhulanov VV (2009) One-coordinate X-ray detector OD-3M. Nuclear Instrum Methods Phys Res Sect A Accel Spectrom Detect Assoc Equip 603:76–79. https://doi.org/10.1016/j.nima.2008.12.164

36. Szajerski P, Bogobowicz A, Gasiorowski A (2020) Cesium retention and release from sulfur polymer concrete matrix under normal and accidental conditions. J Hazard Mater 381:121180. https://doi.org/10.1016/j.jhazmat.2019.121180

37. Niwa E, Sato K, Yashiro K, Mizusaki J (2019) High-temperature gravimetric study on the kinetics of the formation of $SrTiO_3$ by solid state reaction of $SrCO_3$ and TiO_2. ECS Trans 16:205–210. https://doi.org/10.1149/1.3224758

38. Dermatas D, Moon DH, Menounou N, Meng X, Hires R (2004) An evaluation of arsenic release from monolithic solids using a modified semi-dynamic leaching test. J Hazard Mater 116:25–38. https://doi.org/10.1016/j.jhazmat.2004.04.023